

# Resonance line-profile calculations based on hydrodynamical models of cataclysmic variable winds.

Daniel Proga

LHEA, GSFC, NASA, Code 662, Greenbelt, MD 20771  
Presently at JILA, University of Colorado, Boulder, CO 80309-0440; proga@colorado.edu

Timothy R. Kallman

LHEA, GSFC, NASA, Code 662, Greenbelt, MD 20771; tim@xstar.gsfc.nasa.gov

Janet E. Drew & Louise E. Hartley

Imperial College of Science, Technology and Medicine, Blackett Laboratory, Prince Consort Road, London, SW7 2BZ, UK; j.drew@ic.ac.uk, le.hartley@ic.ac.uk

## ABSTRACT

We describe a method of calculating synthetic line profiles using a generalized version of the Sobolev approximation. We apply this method to calculate line profiles predicted by the models of two-dimensional line-driven winds from luminous disks due to Proga, Stone & Drew. We describe the main properties of the model line profiles and compare them with recent HST observations of the cataclysmic variable IX Vel. The model wind consists of a dense, slow outflow that is bounded on the polar side by a high-velocity stream. We find that these two wind components produce distinct spectral features. The fast stream produces profiles which show features consistent with observations. These include the appearance of the classical P-Cygni shape for a range of inclinations, the location of the maximum depth of the absorption component at velocities less than the terminal velocity, and the transition from net absorption to net emission with increasing inclination. However the model profiles have too little absorption or emission equivalent width compared to observed profiles. This quantitative difference between our models and observations is not a surprise because the line-driven wind models predict a mass loss rate, mostly due to the fast stream, that is lower than the rate required by the observations. We note that the model profiles exhibit a double-humped structure near the line center which is not echoed in observations. We identify this structure with a non-negligible redshifted absorption which is formed in the slow component of the wind where the rotational velocity dominates over expansion velocity. We conclude that the next generation of disk wind models, developed for application to CVs, needs to yield stronger wind driving out to larger disk radii than do the present models.

*Subject headings:* accretion disks – outflows – novae, cataclysmic variables – methods: numerical

## 1. Introduction

Outflows appear to be a common feature of many types of accreting compact objects. In the case of cataclysmic variables (CVs), key evidence for outflows comes from P-Cygni profiles of strong UV lines such as C IV  $\lambda 1549$ . But until recently there was no *ab initio* dynamical model of these outflows, and interpretation of data was limited to fitting observed profiles to synthetic profiles calculated from kinematic models. This situation has changed with the advent of numerical models for the hydrodynamics of disk winds, and it is now possible to calculate synthetic profiles from them. This is what we set out to do in this paper.

The International Ultraviolet Explorer (IUE) satellite (Boggess et al. 1978) first discovered that CVs exhibit P Cygni type line profiles (Heap et al. 1978). These were mainly identified in low resolution ( $\lambda/\Delta\lambda \sim 300$ ) IUE spectra where absorption troughs extending bluewards over  $\sim 5000 \text{ km s}^{-1}$  were noted (e.g., Cordova & Mason 1984; Drew 1990). This phenomenon is attributed to high-velocity winds by analogy with OB stars (e.g., Krautter et al. 1981). The affected line transitions are without exception, C IV  $\lambda 1549$  and N V  $\lambda 1240$  and, in many instances, Si IV  $\lambda 1397$ . Because the maximum observed wind speeds are often comparable with the escape speed from a WD photosphere, it has been presumed that CV winds are disk winds originating from close to, if not on, the accreting WD (Cordova & Mason 1982).

The particular varieties of CV that most clearly exhibit wind features are the non-magnetic systems in the high state: the dwarf novae (DN) in outburst and nova-like variables (NLs). The main difference between these CV sub-types is in their secular light curves: DN undergo brightness increases (outbursts) of several magnitudes at quasi-regular intervals, whereas NLs are more stable objects staying always in a high state. The outbursts in DN are understood as rapid changes in the physical structure of the accretion disk – the instabilities being related to changes in the mass accretion rate (Cannizzo 1993).

The observed low-resolution UV profile shape depends sensitively on the inclination angle of the system. Observed profiles range from broad shortwardshifted absorption, with or without redshifted emission, in cases of low-to-intermediate inclination angles ( $\leq 60^\circ$ ), to Doppler-broadened emission profiles in luminous CVs viewed almost edge on. This behavior is consistent with line formation mainly by resonant scattering in a somewhat bipolar disk wind (Drew & Verbunt 1985, Drew 1987).

The UV observations have also shown that CV mass loss signatures can be very sensitive to luminosity. During declines of DN from maximum light, the UV continuum decays by a factor of  $\gtrsim 2$ ; the blueshifted absorption prominent at the maximum light often nearly vanishes during the decline (e.g., Woods et al. 1992). Analogous behavior has been noted in some NLs as their brightness level varies (e.g., Mason et al. 1995).

Other properties of the UV resonance line profiles that are likely related to winds have been observed in the small fraction of highly-inclined non-magnetic CV that exhibit deep continuum eclipses. For example, weak UV line eclipses or even line brightenings were found at times of continuum eclipse in UX UMa (King et al. 1983), RW Tri (Cordova & Mason 1985) and OY Car (Naylor et al. 1988). These weak line eclipses indicate either a size of emission line region larger than the secondary star, or an out-of-eclipse line profile that is a spatially unresolved superposition of a net absorption component on a stronger emission feature (Drew 1987). A further observed property of the emission lines in eclipsing systems is the narrowing of the UV resonance lines during the eclipse (OY Car: Naylor et al. 1988, V347 Pup: Mauche et al. 1994, and UX UMa: Mason et al. 1995).

Research on the supersonic outflows in CVs has nearly closed a circle in science: from observations and

simple phenomenological models through sophisticated kinematic models to first generation of dynamical models. There have been many successes in this process; for example, the kinematic models developed by Drew (1987), Mauche & Raymond (1987) and later by Shlosman, Vitello & Mauche (1996) and by Knigge & Drew (1997) provide a point of comparison for dynamical theories of outflows. Dynamical models appealing to radiation pressure driving have met with qualitative success in explaining some observed disk wind properties (Pereyra, Kallman & Blondin 1997; Proga, Stone & Drew 1998, 1999, hereafter PSD 98 and PSD 99; Proga 1999; Feldmeier & Shlosman 1999; Feldmeier, Shlosman & Vitello 1999; Pereyra, Kallman & Blondin 2000). Important outcomes of the hydrodynamical simulations were (i) the mass loss rate’s practical independence of the radiation field geometry – it is first and foremost a function of total system luminosity, (ii) the discovery of unsteady flow in models where the disk radiation field dominates over any contribution from the central accreting object. To bring closure of the scientific circle even nearer, the main objective here is to calculate synthetic line profiles directly from the line-driven disk wind models of PSD 99 and to critically compare them with relevant high quality UV observations.

Our focus shall be on assessing the gross properties of the line profiles - such as the strength and shape of the blueshifted absorption. In Section 2, we briefly review the past work in the field of winds in CVs and then describe our method of calculating line profiles, using a generalized Sobolev approximation. The results are presented in Section 3. In Section 4, we discuss key aspects of the synthetic line profiles and make comparisons with recent observations.

## 2. Method

Recently numerical hydrodynamic models of 2.5-D, time-dependent radiation driven disk winds have been constructed for application to, in the first instance, CV disk winds (Pereyra, Kallman & Blondin 1997; PSD 98; PSD 99; Proga 1999). The primary outcome of these studies is the confirmation that radiation-pressure due to spectral lines can produce a supersonic, biconical outflow from an accretion disk in nMCVs. Additionally, PSD 98 and PSD 99 found that regardless of the radiation geometry, the two-dimensional structure of the wind consists of a dense, slow outflow that is bounded on the polar side by a high-velocity stream (respectively ‘slow wind’ and ‘fast stream’, for short; see e.g., Figure 2 in PSD 99).

Applying PSD 98 and PSD 99’s dynamical models to CVs one finds that radiation driving can produce disk winds consistent with the following observed properties of CV winds:

- (1) the flow is biconical rather than equatorial as required by the absence of blueshifted line absorption from the spectra of eclipsing high-state nMCV,
- (2) the wind terminal velocity is comparable to the escape velocity from the surface of the WD,
- (3) the spectral signatures of mass loss show a sharp cut-off as the total luminosity in DN declines away from maximum light through the regime theoretically identified as likely to be critical.

Additionally, line-driven disk wind models may explain the highly unsteady and continuously variable nature of the supersonic outflows in the NL binaries BZ Cam and V603 Aql (Prinja et al. 2000a; b). The presence of a slow, dense transition region between disk photosphere and outflow in V347 Pup and UX UMa (Shlosman, Vitello & Mauche 1996; Knigge & Drew 1997) may also be accommodated within these same models. These successes of the line-driven wind model are encouraging and provide the motivation for its closer examination.

## 2.1. Line-profile Calculations

We restrict our attention to the case of a representative UV resonance transition of a light ion such as C IV or Si IV. The assumed abundance and atomic data are appropriate to the C IV 1549Å transition treated as a singlet. The profiles synthesized on this basis allow us to address the main issues of this paper.

As in the hydrodynamical calculations, we apply a generalized Sobolev approximation (Sobolev 1957; Rybicki & Hummer 1978, 1983) in treating spectral line transport through a wind. Our calculations are similar to those by Shlosman & Vitello (1993). The main differences are (i) we base our calculation on numerical hydrodynamical wind models whereas Shlosman & Vitello used kinematic wind models (ii) we allow both the white dwarf and the accretion disk to radiate but neglect the boundary layer whereas Shlosman & Vitello considered the disk, white dwarf and boundary layer as a source of radiation (iii) we assume the wind ionization state whereas Shlosman & Vitello calculated the photoionization of the wind in an optically thin approximation. A minor technical difference between our approach and that of Shlosman & Vitello is that we use spherical polar coordinates  $(r, \theta, \phi)$  while they used cylindrical coordinates  $(R, Z, \phi)$ . We form the three-dimensional computational grid by rotating the spatial  $(r, \theta)$  grid in the  $\phi$  direction in the same way as in the hydrodynamical calculations used as input..

Below is a summary of our method. The radiation propagates in an axisymmetric system with a fully three-dimensional velocity field  $(v_r, v_\theta, v_\phi)$ . We define the monochromatic specific luminosity as

$$L_\nu \equiv \int I_\nu(\hat{n}) dA, \quad (1)$$

where  $I_\nu(\hat{n})$  is the intensity at an arbitrary point along the unit vector  $\hat{n}$  pointing toward the observer. We define a surface element,  $dA$  in the plane of the sky normal to  $\hat{n}$ . In the Sobolev approximation, it is possible to analyze the radiation transport as if all the contributions to the formation of a spectral line at any given frequency occurred locally. In particular, along a given ray the intensity at frequency  $\nu$  does not change at all, except at certain discrete resonance points, where the material has just the right Doppler shift to allow it to absorb or emit. These points occur wherever the line-of-sight velocity  $v_l \equiv \mathbf{v} \cdot \hat{n}$  satisfies the resonance condition:

$$(\nu - \nu_0)/\nu_0 = v_l/c. \quad (2)$$

To calculate the observed line profile, we need to compute the intensity that emerges from the resonance region,

$$I_\nu^{emg} = I_\nu^{inc} \exp\left(-\sum_{i=1}^N \tau_i\right) + \sum_{j=1}^N s_j [1 - \exp(-\tau_j)] \exp\left(-\sum_{i=1}^{j-1} \tau_i\right), \quad (3)$$

where  $s$  is the line source function and  $I_\nu^{inc}$  is the incident intensity due to a disk or stellar surface. The incident intensity is non-zero at a point  $\mathbf{r}$  if  $\hat{n}$  originates on the disk or star surface. The factor  $\exp(-\sum_i \tau_i)$  accounts for non-local effects in a generalized Sobolev approximation: the term  $\tau_i$  is the line optical depth at a possible intervening resonance velocity surface between the point  $\mathbf{r}$  and the observer. In the original version of the Sobolev approximation, the flow velocity along a line of sight is assumed to be monotonic and thus only one resonance surface is considered, i.e.,  $N = 1$  or  $0$  and  $\exp(-\sum_{i=1}^{j-1} \tau_i) = 1$ . Following Rybicki & Hummer (1983), we will refer to the first term on the RHS of eq. 3 as the surface contribution and the second term as the volume contribution to the emergent intensity. These two contributions can be treated separately.

Rybicki & Hummer (1983) showed that the area integral of the terms in the emergent intensity which are linear in the values of the source functions can be replaced by a volume integral,

$$L_\nu^v = \int j_\nu(\mathbf{r}) p_\nu(\mathbf{r}, \hat{n}) d\mathbf{r}^3, \quad (4)$$

where  $j_\nu$  is the emission coefficient, and  $p_\nu$  is the directional escape probability for a photon emitted at point  $\mathbf{r}$  in direction  $\hat{n}$  and frequency  $\nu$ . Equation 4 represents the scattered emission of the resonance line. In the Sobolev approximation, the emission coefficient can be expressed as

$$j_\nu = k(\mathbf{r}) s(\mathbf{r}) \delta(\nu - \nu_0 - \nu_c v_l / c), \quad (5)$$

where  $k$  is the line opacity and  $\delta$  is the Dirac delta function. The escape probability can be written as

$$p_\nu = \frac{1 - \exp[-\tau(\mathbf{r}, \hat{n})]}{\tau(\mathbf{r}, \hat{n})} \exp\left(-\sum_{i=1}^{j-1} \tau_i\right). \quad (6)$$

The optical depth can be approximated by the Sobolev optical depth as

$$\tau(\mathbf{r}, \hat{n}) = \frac{kc}{|dv_l/dl|}, \quad (7)$$

where  $dv_l/dl$  is the velocity gradient along  $\hat{n}$  and may be written as

$$\frac{dv_l}{dl} = Q \equiv \sum_{i,j} \frac{1}{2} \left( \frac{\delta v_i}{\delta r_j} + \frac{\delta v_j}{\delta r_i} \right) n_i n_j = \sum_{i,j} e_{ij} n_i n_j, \quad (8)$$

where  $e_{ij}$  is the symmetric rate-of-strain tensor. Expressions for the components of  $e_{ij}$  in the spherical polar coordinate system are given in Batchelor (1967). To compute the line optical depth, we use the atomic data for the C IV  $\lambda 1549$  transition (i.e. we set the oscillator strength to 0.1911).

To calculate the line opacity, we need to calculate the number density of the absorbing and scattering ions:

$$n_{ion}(\mathbf{r}) = \frac{\rho(\mathbf{r})}{\mu_p m_p} A \xi_{ion}, \quad (9)$$

where  $\rho$  is the mass density,  $m_p$  is the proton mass,  $\mu_p$  is the mean molecular weight per proton,  $\xi_{ion}$  is the ion fraction, and  $A$  is the abundance of a given element with respect to hydrogen assumed to be  $3 \times 10^{-4}$ . We also assume that the ionization stage of our typical element is constant and set both  $\mu_p$  and  $\xi_{ion}$  to unity. Thus the number density of the absorbing and scattering ions depends on position only through the mass density.

Although we take into account non-local coupling caused by non-radial velocity fields while calculating the escape probability we ignore this coupling while calculating the source function. In other words, we calculate the source function assuming that only a single resonance velocity surface exists – this is known as the disconnected approximation (Marti & Noerdlinger 1977). We express the source function as

$$s(\mathbf{r}) = \frac{\langle \beta_{\nu_0} I_{\nu_0} \rangle_\Omega}{\langle \beta_{\nu_0} \rangle}, \quad (10)$$

where  $\langle \beta_{\nu_0} I_{\nu_0} \rangle_\Omega$  is the angular averaged intensity from the radiative source (a disk, a star or both) weight by the escape probability defined as

$$\langle \beta_{\nu_0} I_{\nu_0} \rangle_\Omega = \frac{1}{4\pi} \oint_\Omega p_{\nu_0} I_{\nu_0}^{inc} d\Omega, \quad (11)$$

where  $\Omega$  is the solid angle subtended by the disk and star. The term  $\langle \beta_{\nu_0} \rangle$ , in eq. 10, is the angular averaged escape probability defined as

$$\langle \beta_{\nu_0} \rangle = \frac{1}{4\pi} \oint_{4\pi} p_{\nu_0} d\Omega. \quad (12)$$

We use the disconnected approximation because it is simple to implement in the code and the resultant equations can be solved relatively quickly. We note that the complications resulting from implementing fully the non-local effects within the Sobolev approximation spoil the simplicity of the Sobolev approximation so it is better to use another method to treat the line transport, such as a Monte Carlo method that allows an exact solution. At this stage, where we calculate line profiles based on the hydrodynamical models for the first time, an approximate simple method suffices to illustrate the gross properties of the profiles. We also note that we do not use the thermal part of the source function because it is negligible at the temperature we consider.

To calculate the source function at any location, it is first necessary to specify the disk and star emergent radiation intensities. To do this we adapt the formalism of PSD 99 (see also PSD 98). For the frequency-integrated disk intensity of the disk at radius  $r_D$ , we use the  $\alpha$ -disk form (e.g., Pringle 1981):

$$I_D(r_D) = \frac{3GM_*\dot{M}_a}{8\pi^2 r_*^3} \left\{ \frac{r_*^3}{r_D^3} \left( 1 - \left( \frac{r_*}{r_D} \right)^{1/2} \right) + \frac{x}{3\pi} \left( \arcsin \frac{r_*}{r_D} - \frac{r_*}{r_D} \left( 1 - \left( \frac{r_*}{r_D} \right)^2 \right)^{1/2} \right) \right\}, \quad (13)$$

where  $r_D$  is the disk radius,  $M_*$  and  $r_*$  are the mass and radius of the central star,  $\dot{M}_a$  is the accretion rate through the disk (Shakura & Sunyaev 1973). We include the effects of the irradiation of a disk by a star for  $x > 0$  where  $x$  is defined as the ratio between the stellar luminosity  $L_*$  and the disk luminosity,  $L_D$  (PSD 98). For radiation from a spherical, isothermal star, the frequency-integrated intensity may be written:

$$I_* = \frac{L_*}{4\pi^2 r_*^2} = x \frac{GM_*\dot{M}_a}{8\pi^2 r_*^3}. \quad (14)$$

We assume that both the disk and star radiate isotropically. Then we calculate the intensity emerging from the the disk at a frequency  $\nu$  and radius  $r_D$  as the blackbody intensity,  $B_\nu$  at the temperature  $T_D(r_D) = (\pi I_D(r_D)/\sigma)^{1/4}$ . For the radiation from the star, the frequency-dependent intensity is given as the blackbody intensity at the temperature  $T_* = (\pi I_*/\sigma)^{1/4}$ .

We evaluate both integrals,  $\langle \beta_{\nu_0} I_{\nu_0} \rangle_\Omega$  and  $\langle \beta_{\nu_0} \rangle$ , using a modified version the numerical method from PSD 99 to evaluate the contribution to the line force due to the disk and star based on the integration over a solid angle (see Sect. 3 in PSD 99). In particular, we split the integration of  $\beta_{\nu_0} I_{\nu_0}$  over  $\Omega$  into the integration over the stellar solid angle,  $\Omega_*$ , so  $I_\nu^{inc} = B_\nu(T_*)$  and the disk solid angle,  $\Omega_D$  so  $I_\nu^{inc} = B_\nu(T_D)$ . We take into account the effects due to shadowing of the disk by the star, and occultation of the star by the disk, by properly defining the limits of integration for each.

Having evaluated the values of the integrand in eq. 4 at hydrodynamical grid points, we numerically sum up the contribution to the scattered emission over the volume occupied by the hydrodynamical computational domain. The Dirac delta function in the emission coefficient allows the volume integral to be reduced to an integral over  $r$  and  $\theta$ . For a given point  $(r, \theta)$  to be included in the integral, there must be at least one angle,  $\phi_{res}$  for which the  $\delta$  function does not vanish. As discussed by Shlosman & Vitello, for each value of the  $(r, \theta)$  [or equivalently  $(R, Z)$ ] coordinates there are either two, one or zero solutions for

the  $\phi_{res}$ -value that satisfy the resonance condition. For each resonance point, we follow along  $\hat{n}$  and reduce the contribution of this resonance point to the scattered emission by a factor of  $\exp[-\tau_i]$  whenever the ray defined by this resonance point and  $\hat{n}$  crosses another resonance velocity surface.

We calculate the surface contribution from the disk and star,  $L_\nu^s$  to the luminosity,  $L_\nu$  at the frequency  $\nu$  as

$$L_\nu^s = \int dA I_\nu^{inc} \exp\left(-\sum_{i=1}^N \tau_i\right). \quad (15)$$

This equation represents the direct continuum radiation from the source. For each ray from the disk or star surface we follow along  $\hat{n}$  and reduce the incident intensity by a factor of  $\exp[-\tau(\mathbf{r}, \hat{n})]$  whenever the ray crosses a resonance velocity surface.

## 2.2. Wind Models

For completeness we briefly describe the key elements, assumptions and parameters of the hydrodynamical models we will use to calculate line profiles. See PSD 99 and PSD 98 for the full description.

In the hydrodynamical models, PSD 99 assumed that an optically-thick, Keplerian disk surrounds a non-rotating white dwarf. The disk is flat and geometrically thin in the sense that its radiation is emitted from the disk mid-plane. The disk intensity is assumed to be direction independent. The main input parameters for the 2.5 dimensional line-driven wind model are: the mass accretion rate through the disk, and the stellar mass, radius and luminosity. PSD 99 calculated several wind models for various  $\dot{M}_a$  and  $L_*$  for  $M_* = 0.6 M_\odot$  and  $r_* = 8.7 \times 10^8$  cm. For these stellar parameters, the Keplerian velocity at  $r = r_*$ , is  $v_o = 3017$  km s<sup>-1</sup>.

To calculate the structure of a wind from the disk, PSD 99 took into account stellar gravity, gas pressure effects, rotational and radiation forces. PSD 99 held the sound speed constant at 14 km s<sup>-1</sup> in the isothermal equation of state. PSD 99 used the Castor, Abbott, Klein (1975, hereafter CAK) force multiplier to calculate the line-driving force. In this approximation, a general form for this force at a point defined by the position vector  $\mathbf{r}$  is

$$\mathbf{F}^{rad,l}(\mathbf{r}) = \oint_{\Omega} M(t) \left( \hat{n} \frac{\sigma_e I(\mathbf{r}, \hat{n}) d\Omega}{c} \right) \quad (16)$$

where  $I$  is the frequency-integrated continuum intensity in the direction defined by the unit vector  $\hat{n}$ , and  $\Omega$  is the solid angle subtended by the disk and star at the point W. The term in brackets is the electron-scattering radiation force,  $\sigma_e$  is the mass-scattering coefficient for free electrons, and  $M(t)$  is the force multiplier – the numerical factor which parameterizes by how much spectral lines increase the scattering coefficient. In the Sobolev approximation,  $M(t)$  is a function of the optical depth parameter

$$t = \frac{\sigma_e \rho v_{th}}{|dv_l/dl|}, \quad (17)$$

where  $v_{th}$  is the thermal velocity.

PSD 99 adopted the CAK analytical expression for the force multiplier as modified by Owocki, Castor

& Rybicki (1988, see also PSD 98)

$$M(t) = kt^{-\alpha} \left[ \frac{(1 + \tau_{max})^{(1-\alpha)} - 1}{\tau_{max}^{(1-\alpha)}} \right] \quad (18)$$

where  $k$  is proportional to the total number of lines,  $\alpha$  is the ratio of optically thick to optically-thin lines,  $\tau_{max} = t\eta_{max}$  and  $\eta_{max}$  is a parameter related to the opacity of the most optically thick lines. The term in the square brackets is the Owocki, Castor & Rybicki correction for the saturation of  $M(t)$  as the wind becomes optically thin even in the strongest lines, i.e.,

$$\lim_{\tau_{max} \rightarrow 0} M(t) = M_{max} = k(1 - \alpha)\eta_{max}^\alpha.$$

PSD 99 adopted  $k = 0.2$  and imposed an upper limit  $M_{max} = 4400$  for  $\alpha = 0.6$ .

PSD 99's calculations were performed in spherical polar coordinates  $(r, \theta, \phi)$  with  $r = 0$  at the center of the accreting star. Axial symmetry about the rotation axis of the accretion disk ( $\theta = 0^\circ$ ) was also assumed. Thus all quantities were taken to be invariant in  $\phi$ . The standard computational domain was defined to occupy the radial range  $r_* \leq r \leq 10r_*$ , and angular range  $0 \leq \theta \leq 90^\circ$ . The  $r - \theta$  domain was discretized into zones - the standard numerical resolution consisted of 100 zones in each of the  $r$  and  $\theta$  directions, with fixed zone size ratios,  $dr_{k+1}/dr_k = d\theta_l/d\theta_{l+1} = 1.05$ .

### 3. Results of Profile Calculations

We calculate line profiles for four hydrodynamical models from PSD 99, model A ( $\dot{M}_a = 10^{-8} \text{ M}_\odot \text{ yr}^{-1}$ ,  $x = 0$ ), model B ( $\dot{M}_a = \pi \times 10^{-8} \text{ M}_\odot \text{ yr}^{-1}$ ,  $x = 0$ ) model C ( $\dot{M}_a = \pi \times 10^{-8} \text{ M}_\odot \text{ yr}^{-1}$ ,  $x = 1$ ) model D ( $\dot{M}_a = \pi \times 10^{-8} \text{ M}_\odot \text{ yr}^{-1}$ ,  $x = 3$ ). This range of models illustrates the dependence of the disk wind on the disk and stellar luminosities. We note that this sequence of models is a rising sequence in the total system luminosity (see Table 1). To examine the effect of viewing angle on the line profiles, for each disk wind model we compute line profiles for five inclination angles:  $i = 5^\circ, 30^\circ, 55^\circ, 70^\circ$ , and  $85^\circ$ . Examining effects of inclination angle is important because of the strong inclination angle dependence observed in CV spectra. As noted earlier, this inclination dependence has been viewed as the key evidence for a biconical wind associated with a disk rather than a spherical wind associated with a white dwarf. Figure 1 shows the model line profiles obtained after scaling to unit continuum level. We calculate the line profiles at a velocity resolution of  $\sim 16.7 \text{ km s}^{-1}$  that corresponds to a spectral resolution of  $\sim 0.17 \text{ \AA}$ .

As found by PSD 98 (see also PSD 99), there are two kinds of flow that might arise from luminous accretion disks: a complex weak wind and a strong steady wind. We first describe line profiles for a representative example of each of these two types of winds in some detail first (specifically model A in section 4.1 and model C in 4.2). Then we review the effects of varying the disk luminosity and the relative luminosity of the white dwarf (see section 4.3).

Table 1 summarizes the main input parameters of the hydrodynamical disk wind models including the mass accretion rate,  $\dot{M}_a$ , total stellar luminosity relative to the disk luminosity,  $x$  and resultant total system luminosity,  $L_{tot} = L_D + L_* = (1 + x)L_D$ . Additionally, the table lists the fraction of continuum intensity at the line frequency that is due to the disk,  $f_D$ , for various inclination angles, and the gross properties of the disk winds including the mass-loss rate,  $\dot{M}_w$ , characteristic velocity of the fast stream at  $10r_*$ ,  $v_r(10r_*)$  and flow opening angle,  $\omega$ . As in PSD 99, we define the flow opening angle as an angle between the disk equator and the upper envelope of the wind at  $10r_*$ .



### 3.1. A complex weak wind case

First, we present our results for a complex weak wind for which  $\dot{M}_a = 10^{-8} \text{ M}_\odot \text{ yr}^{-1}$  and the white dwarf is assumed to be dark  $x = 0$  (model A). The gross properties of this wind model are: the wind mass loss rate  $\dot{M}_w = 5.5 \times 10^{-14} \text{ M}_\odot \text{ yr}^{-1}$ , the characteristic velocity at  $10 r_*$   $v_r(10 r_*) = 900 \text{ km s}^{-1}$  and flow opening angle,  $\omega = 50^\circ$  (see Table 1 here and table 1 in PSD 99). We note that  $v_r(10 r_*) \sim 1/3 v_o$ .

The five top panels of Figure 1 (i.e. figs. 1a-1e) show the profiles for the model A as a function of  $i$ . The most obvious change in the profiles caused by viewing the disk at different angles is the weakening of the absorption and the strengthening of the scattered emission as inclination angle increases. This strong inclination angle dependence of the line profile is to be expected for a bipolar flow. The width of the line also increases with increasing  $i$  because the line is predominantly broadened by rotation for all inclinations, except for the lowest inclination where the projected rotational velocity is lower than the expansion velocity. The inclination angle affects also the position of the red edge of the absorption which is at the line center for  $i = 5^\circ$  and moves to the red as  $i$  increases for  $i < 85^\circ$ . The fact that, for  $i = 55^\circ$  and  $70^\circ$ , the lines have two maximum absorptions almost equally shifted from the line center to the blue and red shows also that the rotation dominates over expansion in shaping the line profile. Additionally, for  $i = 85^\circ$ , the line is in emission and is double-peaked as expected for a rotating flow (e.g., Rybicki & Hummer 1983). The scattered line emission is very weak for all inclinations except the highest inclination for which the background continuum due to the disk photosphere is significantly reduced by foreshortening. Generally, the line profiles of model A show that indeed the wind is weak in the sense that the wind expansion velocity is low compared to the rotational velocity and the mass loss rate is low.

### 3.2. A strong steady wind case

An example of a strong steady state wind is Model C where  $\dot{M}_a = \pi \times 10^{-8} \text{ M}_\odot \text{ yr}^{-1}$  and the white dwarf radiates at the same rate as the disk  $x = 1$ . The gross properties of the wind are  $\dot{M}_a = 2.1 \times 10^{-11} \text{ M}_\odot \text{ yr}^{-1}$ ,  $\omega = 32^\circ$  and  $v_r(10 r_*) = 3500 \text{ km s}^{-1}$ , the latter being comparable to  $v_o$ . Note that a factor of  $2\pi$  increase in the system luminosity is accompanied by a factor of almost 400 increase in mass loss (see table 1).

The line profiles for a strong steady state wind (fig.1k-1o, i.e. panels in the second from the bottom row) are markedly different from those for the complex weak model. The most striking difference is for high inclination angles. For model A, the line develops a strong, more or less symmetric, double-peaked emission when seen nearly edge-on whereas for model C, the line develops a typical P Cygni profile with a blueshifted absorption and a redshifted emission. Additionally, for the strong steady wind, the line is significantly broader than the weak complex wind at all inclinations. The rotation of the wind does not dominate over expansion in shaping the line. In particular, the shape and strength of the blueshifted absorption is due to expansion. For  $i \lesssim 55^\circ$  there is a redshifted absorption that is broadened by the rotation. The redshifted absorption is weaker and narrower than the expansion-dominated blueshifted absorption. We note a deep narrow absorption at  $v \sim -1000 \text{ km s}^{-1}$  for  $i = 70^\circ$  (Fig. 1n) and at  $v \sim -200 \text{ km s}^{-1}$  for  $i = 85^\circ$  (Fig. 1o). For  $i < 70^\circ$ , line profiles for model A and C are similar in the respect that the scattered emission is weak in both. At  $i = 85^\circ$ , the scattered emission is seen as weaker by the observer for the strong steady model than for the weak complex model because the background continuum emission is stronger in the steady model. At this high inclination, the background continuum of Model C is dominated by the white

dwarf contribution,  $f_* \equiv 1 - f_D = 0.88 > f_D$  (see Table 1). Thus, in contrast with Model A or any model with  $x=0$ , the Model C background continuum is not much reduced by the foreshortening effect.

#### 4. Discussion and comparison with observations

Some of the results shown in the previous section follow from the character of the hydrodynamic models (PSD 98, PSD 99) in a straightforward way. For example, the lack of a strong ordered outflow in models without a white dwarf continuum (model A in the previous section) is consistent with line profiles showing weak, narrow absorption at low inclination and rotation dominated emission at high inclination. Conversely, the models with a white dwarf at least as luminous as the disk produce an ordered radial flow and therefore show broad blueshifted absorption for a range of viewing angles.

A key parameter shaping the total line profile – made up of both scattered emission and absorption – is the ratio of the expansion velocity to the rotational velocity. This can account for the differences in the line profile between models A and B and models C and D. For models with the white dwarf radiation switched on (C and D), the winds are more equatorial and so the rotational velocity decreases along the wind streamlines faster than for models with the white dwarf radiation switched off (A and B). This simple change in the wind geometry reduces the rotational velocity of the flow compared to the expansion velocity. The relatively higher expansion velocity has an important consequence on the scattered emission: for models C and D at high inclination ( $i \gtrsim 60^\circ$ ), the red component of the scattered emission becomes stronger – stronger than the blue component of the emission and stronger than the blueshifted absorption so it is strong enough for the total line to have a P Cygni profile (Fig. 1n, 1s and 1t). This also helps us to understand the complex shape of model C at  $i=70^\circ$  (Figure 1n) as being a transition between the more familiar P-Cygni shape at that inclination of model D (Figure 1s) and the shape affected by scattered blueshifted emission of model B (Figure 1i).

Perhaps the most striking prediction of our calculations is the double-humped structure near line center that persists even in model C and D at intermediate inclinations. We identify this structure with a non-negligible redshifted absorption which is formed in the slow wind where the rotational velocity dominates over expansion velocity. Figure 2 compares the line profiles calculated for model C taken from Figure 1 (Fig. 1k-1o) with line profiles also calculated for model C but with the assumption that the slow wind contributes nothing to the profile near the equator. This change is achieved by setting the ion fraction,  $\xi_{ion} = 0$  for those  $\bar{\omega}$  and  $z$ , that satisfy the condition  $\bar{\omega} > 4r_*$  and  $z < (\bar{\omega} - 4r_*) \tan 30^\circ$ , where  $\bar{\omega}$  and  $z$  are the radius and height cylindrical coordinates (see Fig. 3c in PSD 99 - note that our  $\bar{\omega}$  corresponds to  $r$  on that figure). As one may expect, the model with the transparent slow wind (solid lines) predicts much weaker redshifted absorption and, as a result, the double-humped structure near line center has almost completely disappeared. In particular, the line profile for  $i = 70^\circ$  (Fig. 2d) looks rather more like the smooth P Cygni profile typical of pure expansion.

When compared with the properties of observed line profiles, our models show some features which appear to be qualitatively consistent. These include the appearance of the classical P-Cygni shape for a range of inclinations, the location of the maximum depth of the absorption component at velocities less than the terminal velocity (a requirement discussed in Drew 1987), and the transition from net absorption to net emission with increasing inclination. Whilst this much is encouraging, it is important to move onwards to a more critical, and direct, comparison with spectrally well-resolved observational data. To this

end we can make use of UV spectroscopy described in full by Hartley et al. (in press). In Figure 3, we show a comparison between profiles derived from model C with a transparent slow wind and observations of the CIV 1549Å and SiIV 1403Å transitions in the spectrum of the brightest nova-like variable, IX Vel. We show profiles synthesized for  $i = 60^\circ$  as this is the inclination believed to be appropriate to this binary (Beuermann & Thomas 1990).

In Figure 3, there is clearly too little absorption or emission equivalent width in the synthetic profiles, when compared with the CIV profile. This certainly implies too low a model mass loss rate. This is not a surprise in that the impression emerging from previous work is that mass loss rates in excess of  $1 \times 10^{-10} M_\odot \text{ yr}^{-1}$  are likely to be required (e.g., Drew 1987; Mauche & Raymond 1987; Shlosman & Vitello 1993; Knigge, Woods & Drew 1995; Mauche & Raymond 2000): the mass loss rate for the model shown is just  $2.1 \times 10^{-11} M_\odot \text{ yr}^{-1}$ . It is also no surprise that the observed CIV profile exhibits more redshifted emission than the  $i = 60^\circ$  model prediction – this is also a problem that has been apparent for a while (see e.g. Mauche, Lee & Kallman 1997; Ko et al. 1998 and below).

A more intriguing difficulty is encountered on comparing the observations with the profile synthesized for the flow comprising both the fast stream and the slow wind (dashed line): there is a residue of a rotation-induced double minimum in the latter not present in the former. The structure that is apparent near line center in the observed CIV line profile is not due to rotation – it arises from the doublet nature of the transition (the fine structure splitting is  $484 \text{ km s}^{-1}$ , referred to the blue component). The doublet responsible for the SiIV 1397Å feature is so well-separated ( $\Delta v \sim 1930 \text{ km s}^{-1}$ ) that the red component at 1403Å in IX Vel’s spectrum is a de facto singlet. In Figure 3, the blueshifted absorption in the SiIV profile reassuringly resembles that in CIV, reaching a minimum at the same projected velocity and seemingly sampling the same basic kinematics. Whilst there is a narrow, very-slightly redshifted absorption at  $+100 \text{ km s}^{-1}$  in the SiIV profile, it lacks a counterpart in the blue component of the line and appears to be rather too sharp to attribute to rotation as in the model profiles (see Figure 1 and 2). In making this comparison we have not needed to be careful in our selection of observations – this absence of a rotational effect from observed line profiles appears to be the norm (e.g., Cordova & Mason 1984; Drew 1990; Mason et al. 1995; Prinja & Rosen 1995; Mauche, Lee & Kallman 1997; Prinja et al. 2000a; b).

By making the slow wind transparent, as in the synthesis shown as the solid line in Figure 3, the double minimum apparent near line center is replaced by a more plausible single, blueshifted minimum. This is rather more satisfactory, when compared with the observations.

The significance of this discrepancy and its cure seems clear in one respect: the wind-formed line profiles seen at ultraviolet wavelengths cannot originate in a flow where rotation and poloidal expansion are comparable. The UV lines must trace gas that expands substantially faster than it rotates. This criterion is more likely to be satisfied by angular momentum conserving radiation driven disk winds like those considered here than by constant angular velocity flows (as might be predicted for MHD-driven winds). Accordingly, wholesale abandonment of radiation-driven disk wind models in favour of pure (co-rotating) MHD disk winds could actually make matters worse, rather than better. Regardless of the details of the driving mechanism, the comparison we have made here between model and observation indicates that the seat of the UV wind-formed line profiles cannot be a wind that is both slowly expanding and rapidly rotating.

It is important to note that many of the details of our results depend on details of the assumptions about the disk and microphysics of the wind. For example, the assumed form for the background radiation field inevitably plays a role in the comparison of observed profiles with synthetic profiles based on any

model, kinematic or dynamical. However for line fitting based on radiation-driven wind models, the adopted disk and white dwarf radiation fields are even more important because they determine all wind properties except the initial Keplerian component of motion. In our calculations, we followed PSD 99 and adopted the dependence of the disk radiation on radius according to the standard steady state disk model (e.g., Pringle 1981). This assumption is a good starting point but it should be remembered that actual disks may only be very crudely described by simple theory or they may yield unexpected features such as chromospheric emission. In fact, spectral synthesis models of accretion disk photospheres (e.g., Linnell & Hubeny 1996; Wade & Hubeny 1998; Wade & Orosz 1999) have typically failed to adequately reproduce observed energy distributions where direct comparisons have been made (see e.g. Long et al. 1994). There has been a similar lack of success in past calculations of accretion disk line emission. Specifically, the accounting for both the strengths of and the flux ratios among various emission lines in a large ensemble of observed CVs has not been compelling (Mauche, Lee & Kallman 1997; Ko et al., 1998). These models either miss a crucial physical component or employ an inappropriate physical assumption which affects the predicted line emission. It is for this reason that, in comparing model wind profiles with observation, we concern ourselves more with the absorption component than with the emission.

In our line-profile calculations we also assumed that the ionization fraction of scattering species is constant ( $\xi_{ion}$  is set to unity). A proper allowance for a variation of  $\xi_{ion}$  with position to values less than one can only serve to weaken the overall line profile. (Examples of plots of this potentially very marked positional dependence may be found in the work of Shlosman & Vitello 1993).

Line-driven disk wind models predict that winds driven from an accretion disk without a strong central star yield complex, unsteady outflow (PSD 98 and PSD 99). Therefore we might expect  $\lesssim 100 \text{ km s}^{-1}$  fine structure in blueshifted absorption features and that this fine structure is time-variable. Our results show that line profiles for such complex outflows (model A and model B) are relatively smooth, and that whatever structure is present in the profile at velocities  $\leq 100 \text{ km s}^{-1}$  is small compared with the net absorption on larger velocity scales. This can be attributed partially to the fact the line absorption is nearly saturated in model B (and the non-zero residual flux is due to filling in by emission), and also to the more general point that the density and velocity fluctuations in these wind models are just too fine in spatial scale to imprint on the line profile.

To bridge the gap between the kinematics of the radiation driven models presented here and reality, we will probably need to understand why the wind seen at UV wavelengths should expand with velocities that at least match the rotational velocity over a wide range of radii. There are a few possible changes to the kinematics of the radiation driven models that can improve the situation. For example, it might be that the slow wind present in PSD 99’s models would not contribute to the UV spectrum because its ionization stage is inappropriate. This possibility still requires an increase in the mass loss rate in the fast stream. Another possibility, which we think is more likely, is that the wind launched at large radii is not slow as PSD 99 predicted but some mechanism quickly accelerates the expansion to a velocity exceeding the local rotation speed. It already seems necessary to bring in e.g., MHD processes to yield higher rates of mass loss (see e.g., Mauche & Raymond 2000; Drew & Proga 2000; Proga 2000). Now we can place a more specific requirement on the as-yet unidentified additional driving: it should accelerate dense material launched by the radiation force at larger radii to an expansion velocity at least comparable to the rotational velocity on a length scale of several white dwarf radii. Increasing the mass loss rate by increasing the wind density, rather than the poloidal velocity, is unworkable because such a wind would produce rotational features even stronger than those obtained here.

ACKNOWLEDGMENTS: The work presented in this paper was performed while DP held a National

Research Council Research Associateship at NASA/GSFC. Computations were supported by NASA grant NRA-97-12-055-154. This paper makes use of observations by the NASA/ESA Hubble Space Telescope, obtained at the Space Telescope Science Institute, which is operated by the Association of Universities for Research in Astronomy, Inc., under NASA contract NAS 5-26555.

## REFERENCES

- Batchelor G.K. 1967, *An Introduction to Fluid Mechanics* (Cambridge: Cambridge University Press)
- Boggess et al. 1978, *Nature*, 275, 37
- Beuermann, K., Thomas, H.-C., 1990, *A&A*, 230, 326
- Castor, J.I., Abbott, D.C., Klein, R.I. 1975, *ApJ*, 195, 157 (CAK)
- Cannizzo J.K. 1993, in *Accretion Disks in Compact Stellar Systems*, ed. J.C. Wheeler, Singapore, World Scientific Publishing, p.6
- Cordova, F.A., Mason K.O. 1982, *ApJ*, 260, 716
- Cordova, F.A., Mason K.O. 1984, *MNRAS*, 206, 874
- Cordova, F.A., Mason K.O. 1985, *ApJ*, 290, 671
- Drew, J.E. 1987, *MNRAS*, 224, 595
- Drew, J.E. 1990, in *Physics of Classical Novae*, Lecture Notes in Physics 369, Springer-Verlag, Berlin, p. 228
- Drew, J.E. & Verbunt, F. 1985, *MNRAS*, 213, 191
- Feldmeier, A., Shlosman, I. 1999, *ApJ*, 526, 344
- Feldmeier, A., Shlosman, I., Vitello, P.A.J 1999, 526, 357
- Heap, S. R. et al. 1978, *Nature*, 275, 385
- King A.R., Frank, J., Jameson, R.F., Sherrington, M.R. 1983, *MNRAS*, 203, 677
- Knigge, C., Drew, J.E. 1997, *ApJ*, 486, 445
- Knigge, C., Woods, J.A., Drew, J.E. 1995, *MNRAS*, 273, 225
- Ko, Y., Lee, P. Y., Schlegel, E. M., & Kallman, T. R. 1996, *ApJ*, 457, 363
- Krautter J., Vogt N., Klare G., Wolf B., Duerbeck H. W., Rahe J., Wargau W., 1981, *A&A*, 102, 337
- Linnell, A.P., & Hubeny, I. 1996, *ApJ*, 471, 958
- Long, K.S., Wade, R.A., Blair, W.P., Davidsen, A.F., & Hubeny, I. 1994, *ApJ*, 426, 704
- Marti, F. & Noerdlinger P.D. 1977, *ApJ*, 215, 247
- Mason, K. O., Drew, J. E., Cordova, F. A., Horne, K., Hilditch, R., Knigge, C., Lanz, T., & Meylan, T. 1995, *MNRAS*, 274, 271
- Mauche, C. 1998, in ASP Conf. Ser. 137, *Wild Stars in the Old West: Proceedings of the 13th North American Workshop on Cataclysmic Variables and Related Objects*, ed. S. Howell, E. Kuulkers, & C. Woodward (San Francisco: ASP), 113
- Mauche, C.W., Lee, Y.P., Kallman, T.R. 1997, *ApJ*, 477, 832
- Mauche C.W., Raymond J.C. 1987, *ApJ*, 323, 690

- Mauche C.W., & Raymond J.C. 2000, ApJ, 323, 690
- Mauche, C. W., Raymond, J. C., Buckley, D. A. H., Mouchet, M., Bonnell, J., Sullivan, D. J., Bonnet-Bidaud, J.-M., & Bunk, W.H. 1994, ApJ, 424, 347
- Naylor, T., Bath, G. T., Charles, P. A., Hassall, B. J. M., Sonneborn, G., van der Woerd, H., & van Paradijs, J. 1988, MNRAS, 231, 237
- Owocki, S.P., Castor J.I., & Rybicki, G.B. 1988, ApJ, 335, 914
- Pereyra, N.A., Kallman, T.R., & Blondin, J.M. 1997, ApJ, 477, 368
- Pereyra N.A., Kallman T.R., Blondin J.M., 2000, ApJ, 532, 536
- Pringle J.E. 1981, ARAA, 19, 137
- Prinja, R.K., Knigge, C., Ringwald, F.A., Wade, R.A. 2000, MNRAS, 318, 368, b
- Prinja, R.K., Ringwald, F.A., Wade, R.A., Knigge, C. 2000, MNRAS, 312, 316, a
- Prinja, R.K., Rosen S.R. 1995, MNRAS, 273, 461
- Proga, D. 1999, MNRAS, 304, 938
- Proga, D 2000, ApJ, 538, 684
- Proga, D., Stone J.M., & Drew J.E. 1998, MNRAS, 295, 595 (PSD 98)
- Proga, D., Stone J.M., & Drew J.E. 1999, MNRAS, 310, 476 (PSD 99)
- Rybicki G.B., & Hummer D.G. 1978, ApJ, 219, 654
- Rybicki G.B., & Hummer D.G. 1983, ApJ, 274, 380
- Shakura N.I., & Sunyaev R.A. 1973 A&A, 24, 337
- Shlosman I., & Vitello P.A.J. 1993, ApJ, 409, 372
- Shlosman I., Vitello P.A.J., & Mauche C. W. 1996, ApJ, 461, 377
- Sobolev, V.V. 1957, Soviet Astron.-AJ, 1, 678
- Wade, R.A., & Hubeny, I. 1998, ApJ, 509, 350
- Wade, R.A., & Orosz J.A. 1999, ApJ, 525, 915
- Woods J.A., Verbunt, F., Collier Cameron, A., Drew, J.E., & Pitters, A. 1992, MNRAS, 255, 237

### Figure Captions

Figure 1 – Line profiles for hydrodynamical disk wind models as a function of inclination angle,  $i$ . The values of  $i$  are  $5^\circ$ ,  $30^\circ$ ,  $55^\circ$ ,  $70^\circ$  and  $85^\circ$  (panels in first, second, third, fourth and fifth column, respectively). The panels in the top and second from the top row, a-e and f-j, are both for models with  $x = 0$  but with  $\dot{M}_a = 10^{-8} \text{ M}_\odot \text{ yr}^{-1}$  (model A) and  $\dot{M}_a = \pi \times 10^{-8} \text{ M}_\odot \text{ yr}^{-1}$  (model B), respectively. The panels in the second from the bottom and the bottom row, k-o and p-t, show results for models both with  $\dot{M}_a = \pi \times 10^{-8} \text{ M}_\odot \text{ yr}^{-1}$ , but with  $x = 1$  (model C) and  $x = 3$  (model D). The panels for model A and model B (a-e and f-j) show the effect on the profiles of increasing the disk luminosity alone, while the panels for model B, model C and D (f-j, k-o, and p-t) show the effect of adding in an increasingly larger stellar component ( $x = 0, 1$  and  $3$ ) to the radiation field. The total systems luminosity and therefore the wind mass mass loss rate increase from top to bottom. The choice of input parameters for the hydrodynamical models shown is the same as in Figure 10 of PSD 98 and in Figure 2 in PSD 99. The zero velocity corresponding to the line center is indicated by the vertical line. Note the difference in the velocity and flux ranges in the planes for  $i = 85^\circ$  (fifth column).

Figure 2 – Line profiles for hydrodynamical disk wind model C as a function of inclination angle,  $i$ . The values of  $i$  are as in Figure 1. The figure compares the line profiles for model C from Figure 1 (Fig. 1k-1o), dashed lines here, with the line profiles for model C with the slow wind material between the disk equator and the ‘fast stream’ assumed to be optically thin in the line, solid lines. We define the location of the transparent wedge in the wind using the cylindrical coordinates,  $\bar{\omega}$  and  $z$ , that satisfy the condition  $\bar{\omega} > 4r_*$  and  $z < (\bar{\omega} - 4r_*) \tan 30^\circ$  (see the text for more details).

Figure 3 – Comparison between profiles derived from model C with and without the assumption that a slow wind is transparent (thick solid and thick dashed line, respectively) and observations of the C IV 1549Å and Si IV 1403Å transitions in the spectrum of the brightest nova-like variable, IX Vel (Hartley et al., in press). The synthetic profiles are for the inclination of  $60^\circ$ . For clarity, we renormalized the synthetic profiles so their continuum flux is at 1.25 not at 1.00 as the continuum flux of the observed profiles.



Table 1: Input parameters and main characteristics of the hydrodynamical models used in this paper (see also PSD 99)

model	$\dot{M}_a$ ( $M_\odot \text{ yr}^{-1}$ )	x	$L_{tot}$ $L_\odot$	$f_D(i = 30^\circ)$	$f_D(i = 55^\circ)$	$f_D(i = 70^\circ)$	$f_D(i = 85^\circ)$	$\dot{M}_w$ ( $M_\odot \text{ yr}^{-1}$ )	$v_r(10r_*)$ ( $\text{km s}^{-1}$ )	$\omega$ degrees
A	$10^{-8}$	0	7.5	1.00	1.00	1.00	1.00	$5.5 \times 10^{-14}$	900	50
B	$\pi \times 10^{-8}$	0	23.4	1.00	1.00	1.00	1.00	$4.0 \times 10^{-12}$	3500	60
C	$\pi \times 10^{-8}$	1	46.9	0.78	0.77	0.71	0.12	$2.1 \times 10^{-11}$	3500	32
D	$\pi \times 10^{-8}$	3	93.8	0.63	0.61	0.56	0.08	$7.1 \times 10^{-11}$	5000	16

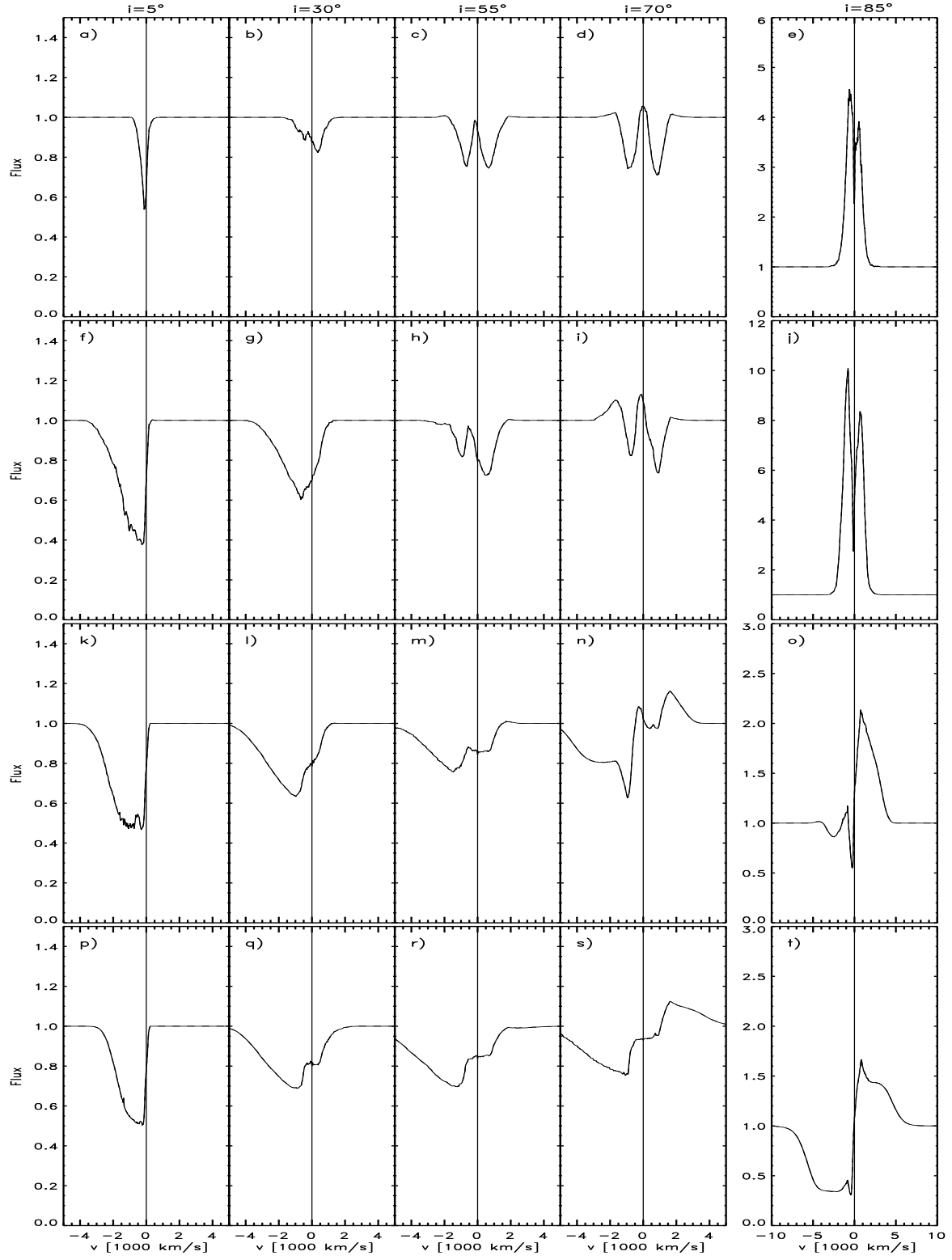


Fig. 1.—

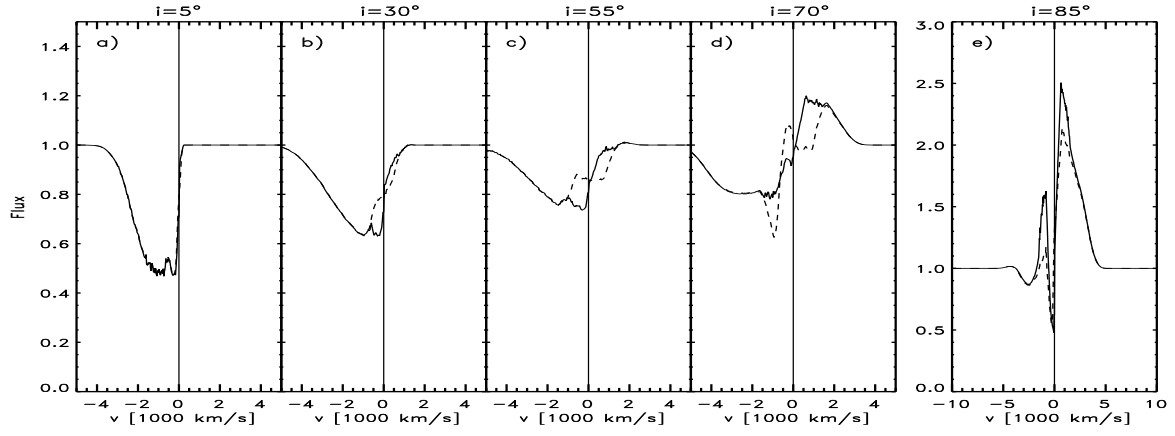


Fig. 2.—

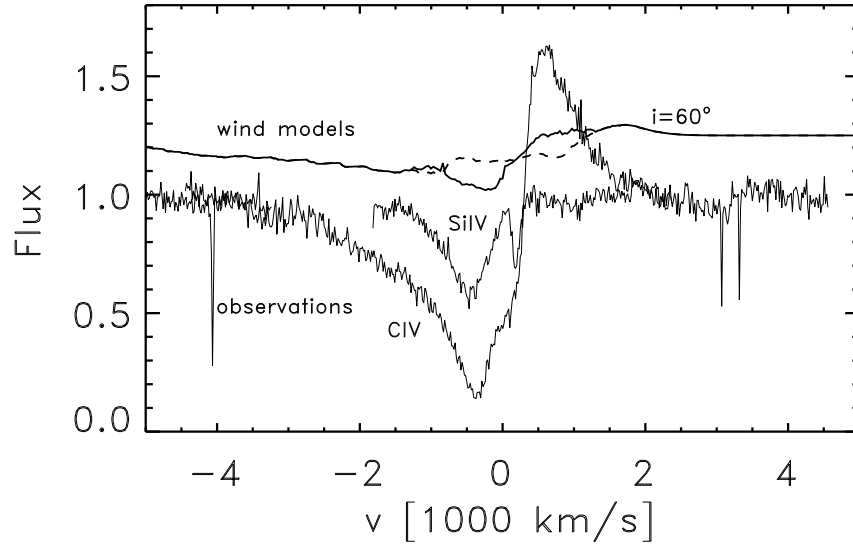


Fig. 3.—